



Influence of deposition procedure on the properties of multiferroic BiFeO₃-based thin films deposited by radio frequency sputtering

O. García-Zaldívar^{1,2} · M. C. Rodríguez-Aranda⁴ · S. Díaz-Castañón³ · F. Calderón-Piñar^{1,2} · F. J. Flores-Ruiz⁵ · J. M. Yáñez-Limón¹

Received: 26 June 2018 / Accepted: 26 October 2018 / Published online: 2 November 2018
© Springer-Verlag GmbH Germany, part of Springer Nature 2018

Abstract

Two samples of Bi_{1-x}Ba_x(Fe_{1-x}Ti_x)O₃ with $x=0.1$ thin films were deposited by RF sputtering method, on commercial indium tin oxide/glass substrates, using different deposition procedures. The effects of deposition conditions on the structural, magnetic and electrical properties of the thin films are studied. X-ray diffraction, scanning electron microscopy (SEM), dielectric and magnetic characterization techniques were performed at room temperature. The results show that the two samples exhibit rhombohedral perovskite structure without the presence of undesired phases of mixed iron bismuth oxides. The SEM micrographs reveal a huge difference in grain size between the films obtained by the two distinct deposition procedure. The analysis of the reflection and transmission spectra in the UV–vis range allowed us to determine the thickness and roughness of thin films synthesized. Also, from this analysis, the optical band-gap energy increases compared with that obtained for this doped compound in volume and with pure BiFeO₃.

1 Introduction

Multiferroics systems have caught the attention of the research community [1–5], mainly due to the impact they would have on the development of new applications. The availability of materials, in which magnetic and electric order coexist, opens a window of possibilities for the development of new technologies with potential applications in

electronics, magnetoelectric sensors and memory devices [6].

Bismuth ferrite (BiFeO₃) continues to attract interest as a multiferroic material due to the coexistence of ferroelectric and ferromagnetic properties above room temperature. From the magnetic point of view, BFO exhibits a canted spin arrangement between near Fe³⁺ ions leading to a local weak ferromagnetism, although the system is antiferromagnetic at macroscopic level due to its spiral spin structure [5, 7]. However, the antiferromagnetic order, the high electrical conductivity and poor phase stability at the sintering temperature are the principal drawbacks in the possible applications of this material.

Two different approaches can be made to overcome these difficulties: (1) doping the system, depending on the ionic radius and valence of dopants, either in the A sites (Bi³⁺ sites) or the B sites (Fe³⁺ sites) of the perovskite structure or in both simultaneously [1–3, 8, 9]; (2) synthesizing the system as a thin films over a substrate of Pt/Ti/SiO₂/Si or SrTiO₃/Si [9–11].

The first approach can effectively improve the thermal stability of the BFO phase during the synthesis step. In this case, the electric conductivity decreases due to the reduction in oxygen vacancies and Fe valence fluctuations via the charge compensation mechanisms introduced by dopants. The second approach improves the thermal stability of

✉ O. García-Zaldívar
osmany.garcia@gmail.com

¹ Centro de Investigación y de Estudios Avanzados del I.P.N. Unidad Querétaro, Libramiento Norponiente No. 2000, Fracc. Real de Juriquilla, C.P. 76230, Querétaro, Qro, Mexico

² Facultad de Física/IMRE, Universidad de La Habana, San Lázaro y L, C.P. 10400, La Habana, Cuba

³ División de Materiales Avanzados, Instituto Potosino de Investigación Científica y Tecnológica, C.P. 78216, San Luis Potosí, Mexico

⁴ Coordinación para la Innovación y Aplicación de la Ciencia y la Tecnología, Universidad Autónoma de San Luis Potosí, S.L.P., Av. Sierra Leona No.550, Col. Lomas 2a. Sección, C.P. 78210, San Luis Potosí, Mexico

⁵ CONACYT-Instituto de Física, Benemérita Universidad Autónoma de Puebla, C.P. J-48, 72570 Puebla, Pue, Mexico

the BFO phase due to the significant reduction in sintering temperature (i.e., around 200 °C lower than that of the bulk sample). Lower sintering temperatures avoid the Bi volatilization, promoting a reduction in oxygen vacancies and Fe valence fluctuations and, accordingly, a reduction in electric conductivity. Additionally, the low thickness of the film permits to reach the high electric fields, needed to achieve polarization switching, with the use of very low applied voltages.

On the other hand, both approaches can improve the magnetic properties of the system via structural distortion (i.e., changes in bonds length, Fe–O–Fe bond angle, FeO₆ octahedral tilting angle or all) caused by dopant incorporation or the strain induced by the substrate in the case of thin films [12]. These distortions cause changes in the cooperative interaction between neighboring magnetic Fe³⁺ ions that can promote the suppression, partial or total, of the spiral spin structure. Additionally, in the case of thin films, net non-zero macroscopic magnetization can be achieved if the thickness of the film is below the modulation length (62 nm) of the spiral spin structure [13].

As the magnetic and/or electric properties, of these systems, are highly dependent on sintering conditions or deposition technique and substrate types, we propose in this work the sintering of thin films using two different deposition procedures over indium tin oxide (ITO)/glass substrates by radio frequency (rf) sputtering. The aim of the present manuscript is addressing the influence of the deposition route, in the modified BFO film with Ba and Ti, on the structural features and magnetic properties of the system. The results are discussed and compared with its bulk counterpart.

2 Experimental details

Bi_{0.9}Ba_{0.1}(Fe_{0.9}Ti_{0.1})O₃ (BBFT) thin films with different deposition procedures were fabricated on commercial ITO/glass substrates by radio frequency (rf) sputtering. The ceramic target of BBFT was sintered by the solid reaction method, from oxides and carbonates [14]. Specifically we use high-purity oxides (Bi₂O₃: 99.9%, BaCO₃: 99%, TiO₂: 99.5%, Fe₂O₃: 99.0%). The powders were ball-milled for 2 h, pressed at 100 MPa and calcined at 700 °C for 1 h. Then, the calcined powders were re-milled for 2 h, pressed in a 2-in. diameter die at a pressure of 200 MPa and sintered at 900 °C during 1/2 h in air. No excess Bi₂O₃ was added during the process.

The films were prepared in two different processes. The first one was deposited, using a single-step deposition, with a substrate temperature of 35 °C for 40 min with a target power supply of 50 W, frequency of 13.56 MHz, 19.8 sccm argon flux and working pressure of 1.8×10^{-2} mBar. These parameters were selected by trial and error until the

deposition procedure was optimized. The film obtained, labeled BBFT-1S, was subjected to an ex situ post-heat treatment of 600 °C, 650 °C and 700 °C for 1 h in air in order to choose the adequate sintering temperature. The samples sintered at 700 °C were chosen for the present study due to its better crystallization and surface quality. The thickness of the layer, obtained by fitting the experimental reflection and transmission spectra in the UV–vis range of thin films, was approximated to 157 nm. The second film was deposited with a substrate temperature of 35 °C for 10 min with a target power supply of 50 W and frequency of 13.56 MHz and 19.8 sccm argon flux. The film was subjected to an ex situ post-heat treatment of 700 °C for 1 h in air. After that, a second layer was deposited in the same conditions with a deposition time of 30 min (in order to achieve the same time deposition that the former film) and an ex situ post-heat treatment of 700 °C for 1 h in air. The total thickness of this film, using a two-step deposition and labeled BBFT-2S, was 132 nm.

The crystalline structure of the films was performed using a Dmax 2100 diffractometer (Rigaku) with Cu K_α radiation ($\lambda = 1.5405 \text{ \AA}$) by grazing incidence diffraction (1° incident angle, 0.02° step resolution, 0.4 s integral time) in the 2θ range. The diffractometer was operated at 40 kV and 30 mA. Surface morphology of the films was studied with an XL30 environmental scanning electron microscope (Phillips) in secondary electron (SE) mode.

The magnetic properties of the samples were measured using an Evercool Physical Properties Measurement System (PPMS P525 Quantum Design) in the VSM mode. The maximum applied field used in the measurements was 30 kOe. The magnetic hysteresis loops of the films were corrected by subtracting the offset background signals (sample holder and ITO/glass substrate) as a function of the applied field. Ferroelectric characterization, using a metal–insulator–metal configuration, was performed in a Radiant precision LC coupled to a voltage amplifier TRek 609E-6 at frequency of 100 Hz. For that purpose, gold electrodes (1 mm diameter) were deposited in the top of the film while the ITO substrate served as a bottom electrode.

Piezoresponse force microscopy (PFM) and switching-PFM (SPFM) measurements were conducted using a Bruker's Dimension Atomic Force Microscopy (AFM) System. Measurements were carried out in an environment of controlled humidity and temperature, < 5% RH, ~ 23 °C.

PFM takes advantage of the inverse piezoelectric effect of a piezo- or ferro- electric material, i.e., expansion and contraction of the material as consequence of an alternating electrical field (sinusoidal ac signal) applied between the conductive probe-tip and the bottom electrode located under the material. Such an expansion and contraction are transmitted into deflection of the AFM probe, which are monitored by a position sensitive device (PSD). Vertical signal

from the PSD is sent to a lock-in amplifier (LIA) which uses the sinusoidal ac signal as a reference. From LIA, amplitude gives information about local piezoelectric strength, whereas the phase contains information about orientation of the ferroelectric domain. PFM contrast is improved by using frequencies corresponding to the contact resonances of the probe. Here, concentric micrometric areas were poled at $\pm 12 V_{dc}$ and the typical operating conditions for PFM were $3 V_{pp}$ at 460 kHz.

In switching PFM (SPFM), the sinusoidal ac signal is mounted on variable-amplitude voltage pulses (dc signal) with a triangular envelope in order to change the orientation of the ferroelectric domains. A pulse consists on one-half with positive or negative dc value (on-field) and the other with null value (off-field). Thus, it is possible to obtain phase-switching and amplitude butterfly loops in the excited and remnant states. An optimal signal-to-noise ratio was achieved by applying contact resonance tracking (CRT) in the on- and off-fields of each pulse. Phase switching and butterfly presented here are an average of ten loops. Typical operating conditions for SPFM assisted by CRT were $3 V_{pp}$ at 450–470 kHz. At least five different locations on the surface of the samples were evaluated with the SPFM technique.

X-ray photoelectron spectroscopy (XPS) of the thin films was performed with an Alpha 110 X-ray Photoelectron Spectrometer (ThermoFisher Scientific) equipped with a monochromatic Al K_{α1} (1.486.7 eV) X-ray source, and a hemispherical electron analyzer with seven channeltrons. The spectrum was captured with a step size of 0.05 eV and pass energy of 20 eV at a takeoff angle of 90° (analyzer with normal incidence to the film). The optical transmission and reflection spectra were captured with a Scientific Computing International (SCI) FilmTekTM3000 spectrometer in the UV–vis spectral range (250–850 nm).

3 Results and discussion

Figure 1 shows the X-ray diffraction patterns of the thin films and target. The patterns, typical of the BFO rhombohedral R3c perovskite structure, are observed in all the samples, including the target. The ITO reflections of the substrate are marked as ∇ (pdf # 89-4598 from ICSD). The identification of the crystallographic family of planes, corresponding to BFO phase, according to (pdf # 86-1518 from ICSD) is presented as well.

As can be observed, the reflections of the thin films are shifted towards higher 2θ angle in comparison to those of the target. An increase in the 2θ angles implies a decrease in the interplanar distances [15]. Hence, this is indicative of a contraction of the unit cell when the system crystallizes as a thin film. Additionally, the intensities of the ITO reflections

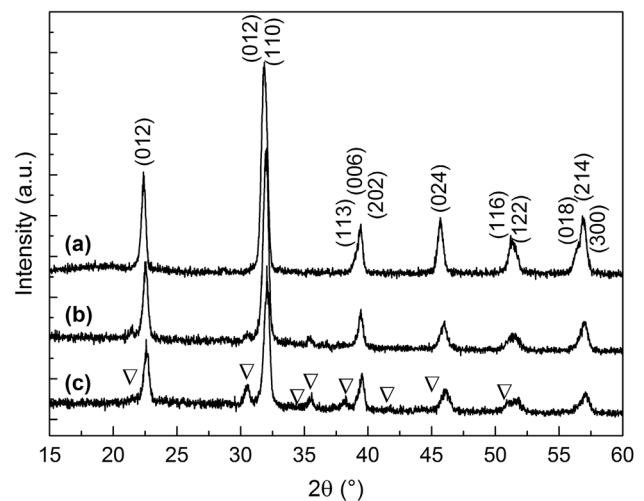


Fig. 1 X-ray diffraction patterns of the measured samples at room temperature. **a** Target, **b** BBFT-1S, **c** BBFT-2S

are higher for the BBFT-2S film, suggesting that this sample is thinner than BBFT-1S. The reduction in films thickness could be related to a better match between the film and the substrate during the crystallization process and to higher grain growth uniformity. The sample BBFT-1S crystallize direct over the ITO substrate, while the BBFT-2S crystallize over a thin layer of the same phase.

Note that for BBFT-2S film, a two-step deposition route was used. In the first step, a thin layer, deposited for 10 min, was sintered at 700 °C for 1 h. This first thin layer could act as a buffer layer, improving the interface coupling and serving as a nucleation center/layer that controls the grain growth uniformity of the subsequent layer deposited over it, that promote the film thickness reduction.

Figure 2 shows SEM images (at two different magnifications) of the films samples in secondary electrons (SE) mode (BBFT-1S: Fig. 2a, c, BBFT-2S: Fig. 2b, d). As can be observed, there is a huge difference in the grain morphology and surface quality between the films obtained by one or two-step deposition route. The sample BBFT-2S presents uniformly distributed submicron grains with well-defined grains and grains boundaries, without showing the formation of pores on the surface.

On the other hand, the SEM micrograph of the BBFT-1S sample shows the formation of abnormally large (above microns) grains which appear to be separated from each other by cracks rather than by proper grain boundaries. In a closer inspection, one can see that these large grains are formed by sub-micron grains, merged with each other without a well-defined grain boundary between them. The cracks between those abnormal grains degrade the insulating properties of the sample; becoming a path for electric current or for the diffusion of deposited electric contacts,

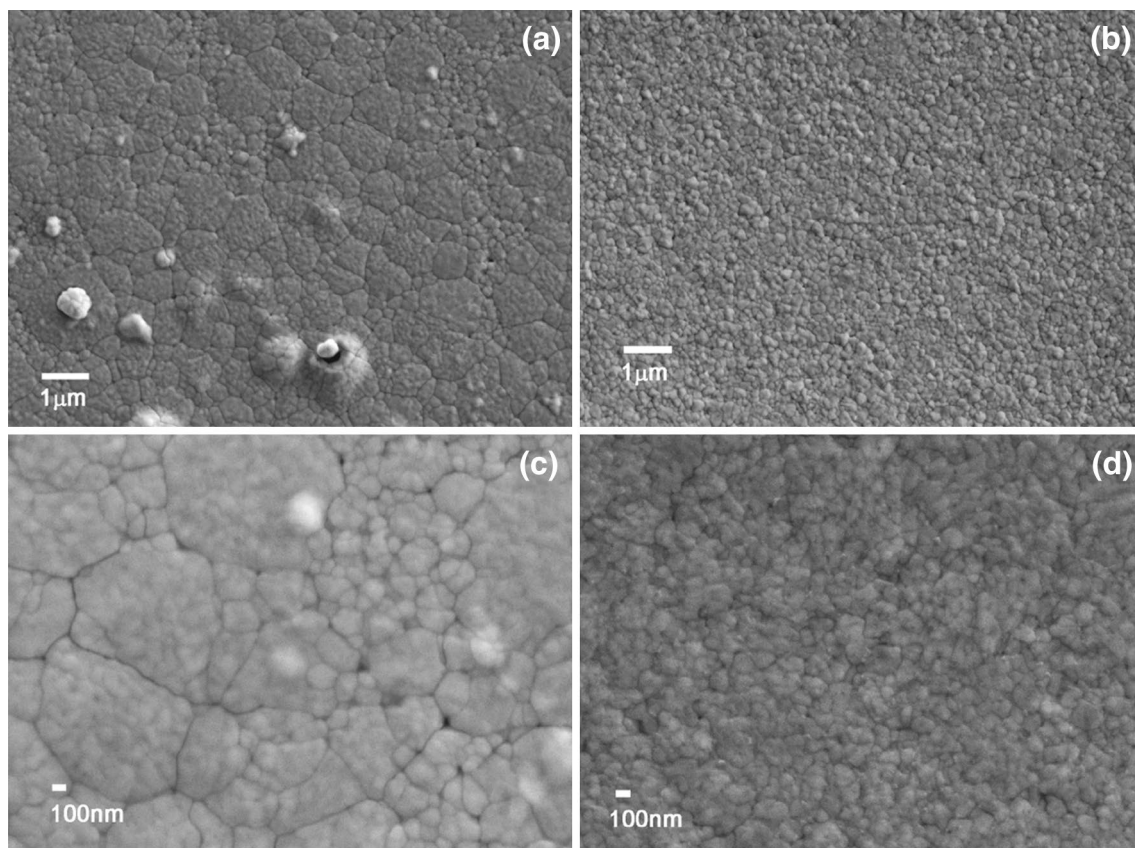


Fig. 2 Scanning electron micrographs of BBFT thin films. **a, c** BBFT-1S. **b, d** BBFT-2S

causing a local short-circuit in the film. Additionally, crater-like holes observed on the film can act as the path for the diffusion of deposited electric contacts too.

Figure 3 shows the optical reflection and transmission spectra of a single layer BBFT-1S and BBFT-2S films with the characteristic interference oscillations in the UV–vis region. The film thickness, d , refractive index, n , extinction coefficient, k , and the energy gap E_g were calculated by minimizing the root-mean-square error (RMSE) value to fit the experimental data to a three-layer optical model.

The model was considered like a BBFT/ITO/glass substrate heterostructure consisting of a bottom ITO layer, an intermediate BBFT layer, and a top layer of BBFT with voids. The voids accounted for the film surface roughness and were specified as volume fraction. The Bruggeman effective medium approximation was employed to describe the top layer. The dispersion relation describing the optical properties of the film, as given by the Lorentz + Drude oscillator model for ITO layer and Lorentz oscillator model for BBFT layer, were also determined. The calculated film thickness was 157 nm for BBFT-1S with a surface roughness of 11 nm and 130 nm of thickness for BBFT-2S with a surface roughness of 4 nm.

The energy band-gap (E_g) of a semiconductor could be inferred from its UV–vis spectra using the following equation:

$$(\alpha h\nu)^n = A(h\nu - E_g),$$

where α corresponds to the absorption coefficient ($\alpha = 4\pi k/\lambda$), $h\nu$ is the photon energy, A is the proportionality constant related to the material, and n represents the index which depends on the electronic transition of the semiconductor (for direct-gap semiconductors, $n=2$) [16]. The E_g is obtained by extrapolating the linear portion of $(\alpha h\nu)^2$ to zero, and the value is determined to be 2.84 eV and 2.82 eV for BBFT-1S and BBFT-2S, respectively. These results are shown in Fig. 4.

The optical band-gap energy of the films is higher than that of reported in [17] for pure BFO ($E_g = 2.05$ eV) or that of the used target, estimated at 2.09 eV by the Kubelka–Munk approximation (inset in Fig. 4). It is a well-known fact that the band-gap increases in thin layers compared to its bulk counterparts [18–20]. With the decrease of the system dimension, increase the surface/volume ratio and, in correspondence, the number of atoms at the surface with an incomplete coordination sphere [19]. Hence, the

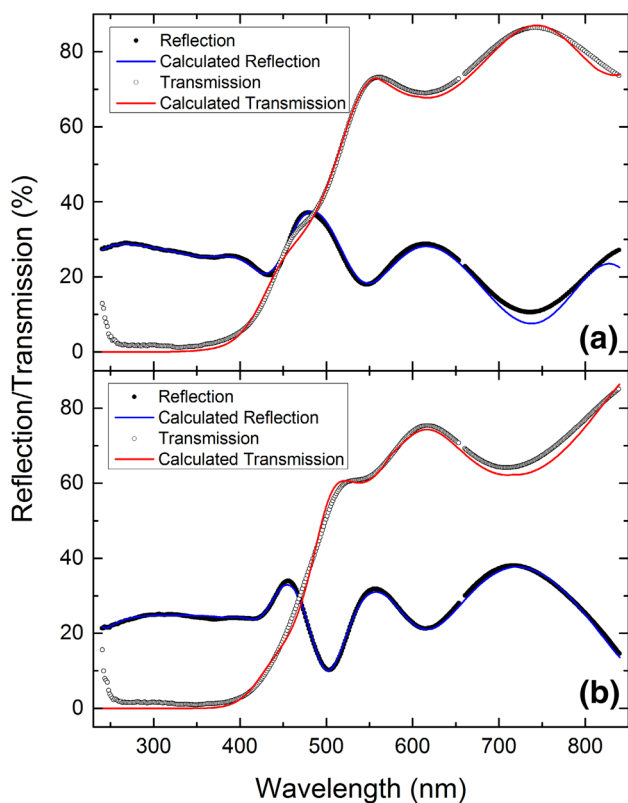
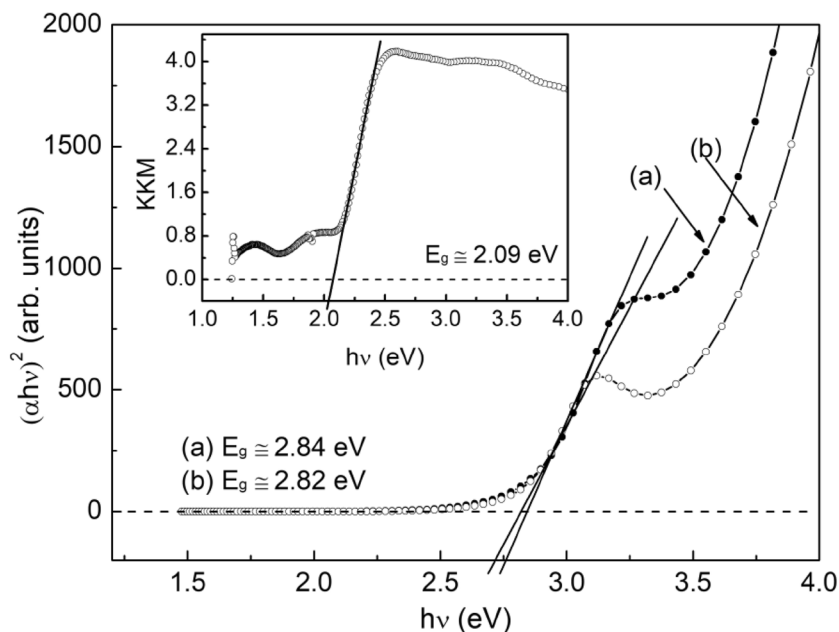


Fig. 3 The measured and fitted reflection and transmission spectra in the UV–vis range for the BBFT thin films **a** BBFT-1S and **b** BBFT-2S

density of states decreases leading to a narrowing of the width of bands (valence and conduction) and consequently an increase in the gap between them. Notice that the grain

Fig. 4 UV–visible absorption spectra of **a** BBFT-1S and **b** BBFT-2S samples. Tauc’s plots to determine the band-gap of the thin films. The inset shows the corresponding spectra of the BFO target using Kubelka–Munk approximation. Horizontal dashed line at y-axis = 0 is a guide to the eyes



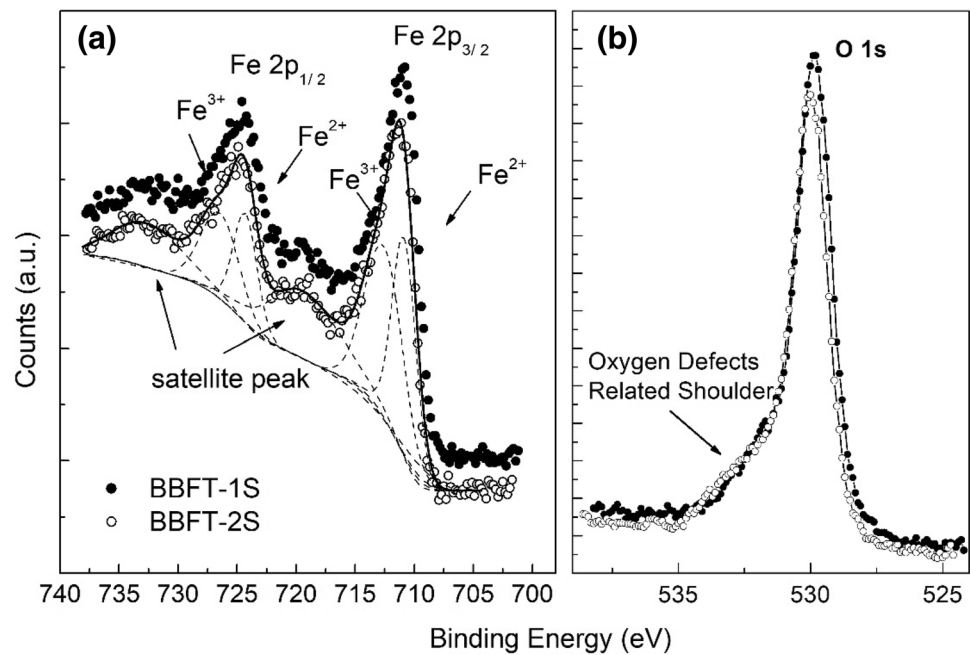
sizes of our films are sub micrometric and in the bulk [14] are over 5 microns.

The XPS narrow scan spectra of Fe 2*p* and O 1*s* are presented in Fig. 5. The 2*p*_{1/2} and 2*p*_{3/2} splitting of Fe 2*p* core level is presented in Fig. 5a. The coexistence of two valence state for Fe (Fe²⁺ and Fe³⁺) was confirmed from the Gaussian deconvolution of the spectra. To accurately account for the two contributions and the contribution of the satellite peaks, all the spectra were fitted (dashed and solid lines, only shown for BBFT-2S for clarity). Fe³⁺ to Fe²⁺ ratio of 55/45 was obtained for both, BBFT-1S and BBFT-2S films, a similar value to that obtained for the target (reported for García-Zaldívar et al. [14]). Hence, the growth process, even when the synthesis temperature is 200 °C below to those used in bulk, has no effect to decrease the Fe³⁺ to Fe²⁺ formation.

The O 1*s* XPS spectrum (Fig. 5b) is composed of one main narrow peak around 529–529.5 cm⁻¹ that can be associated with the of O 1*s* binding energy. The shoulder observed at higher energies in both samples, on the tail of the main peak, is related to oxygen defects [21]. The intensity of this shoulder is lower than that observed in the target [14], an evidence of a lower concentration of oxygen defects in the films. The oxygen defects being one of the main conduction mechanisms in these systems, a reduction in the defects concentration could imply an improvement in the electrical performance of these materials in the form of thin films.

Ferroelectric hysteresis loops of the samples are shown in Fig. 6a. As can be observed, no saturation tendency exists for any of samples, since the values of electric fields well above the coercive field for these materials (between 300 and 500 kV/cm² for other BFO-based materials [22,

Fig. 5 XPS narrow scan spectra of Fe 2p (a) and O 1s (b) for the studied samples



23]) could not be reached. The shape of the curve is similar to that reported for other BFO-based systems, or other conductive ferroelectric systems, when the applied field is below the coercive one and complete domain switching does not occur [24, 25].

In order to evaluate the ferroelectric behavior of films at the nanoscale, local phase-switching and butterfly loops were acquired on the BBFT-1S sample and they are shown in Fig. 6b. Phase switching result indicates that the domain switching in two directions was successfully achieved. On the other hand, butterfly loops allow to determine the coercive bias and the piezoelectric coefficient for both on-field and off-field. Piezoelectric coefficient is around 55 and 30 pm/V for on-field and off-field, respectively. Topography, amplitude and phase PFM images after a ± 12 V_{dc} poling process are shown in Fig. 6c. From these images, amplitude reveals the boundaries of the oppositely poled areas and phase shows a polarization switching phenomenon, which confirm the ferroelectric nature of the studied film at that scale.

The results of ferroelectric hysteresis presented in Fig. 6a are useful to evaluate the electrical performance of both systems. The BBFT-1S sample only reaches a maximum field of 80 kV/cm before dielectric breakdown. On the other hand, BBFT-2S reaches 370 kV/cm without dielectric breakdown. Thus, considering that the band-gap of the two films is similar, these results confirm that the improvement in morphology and surface quality obtained by two-step deposition route becomes crucial in the improvement of the electrical performance of the films.

On the other hand, the magnetic properties are not strongly affected by the deposition route used. The ferromagnetic character of the BBFT-1S and the BBFT-2S thin film is evidenced by a well-defined hysteresis loop (Fig. 7) at room temperature in which the magnetic field was applied parallel or perpendicular direction to the plane of the substrate. Nevertheless, the shape of the loops, in which no saturation tendency exists and in which a slight narrowing of the loop for the fields close to zero is observed, suggests the coexistence of ferro and antiferromagnetic orders in both systems.

In Fig. 7 the hysteresis loop corresponding to the measure in the parallel direction is shown. Measurements in the perpendicular direction (not show here), threw a similar behavior reaffirming the isotropic character of both films. The film thickness (determined from optical UV–vis measurements), were used to calculate the film magnetization (σ) at the maximum applied field of 3 T. Values of σ_{3T} of 60.13 emu/cm³ and 52.70 emu/cm³ were estimated for BBFT-1S and BBFT-2S, respectively. In correspondence, coercive fields of 630 Oe and 850 Oe were determined. The values of both parameters (σ_{3T} , coercive field) are higher than those reported in other BFO-based systems [9, 23].

4 Conclusions

We present the structural, morphological and magnetic results of two thin films obtained both by radio frequency sputtering but with different deposition procedures. The

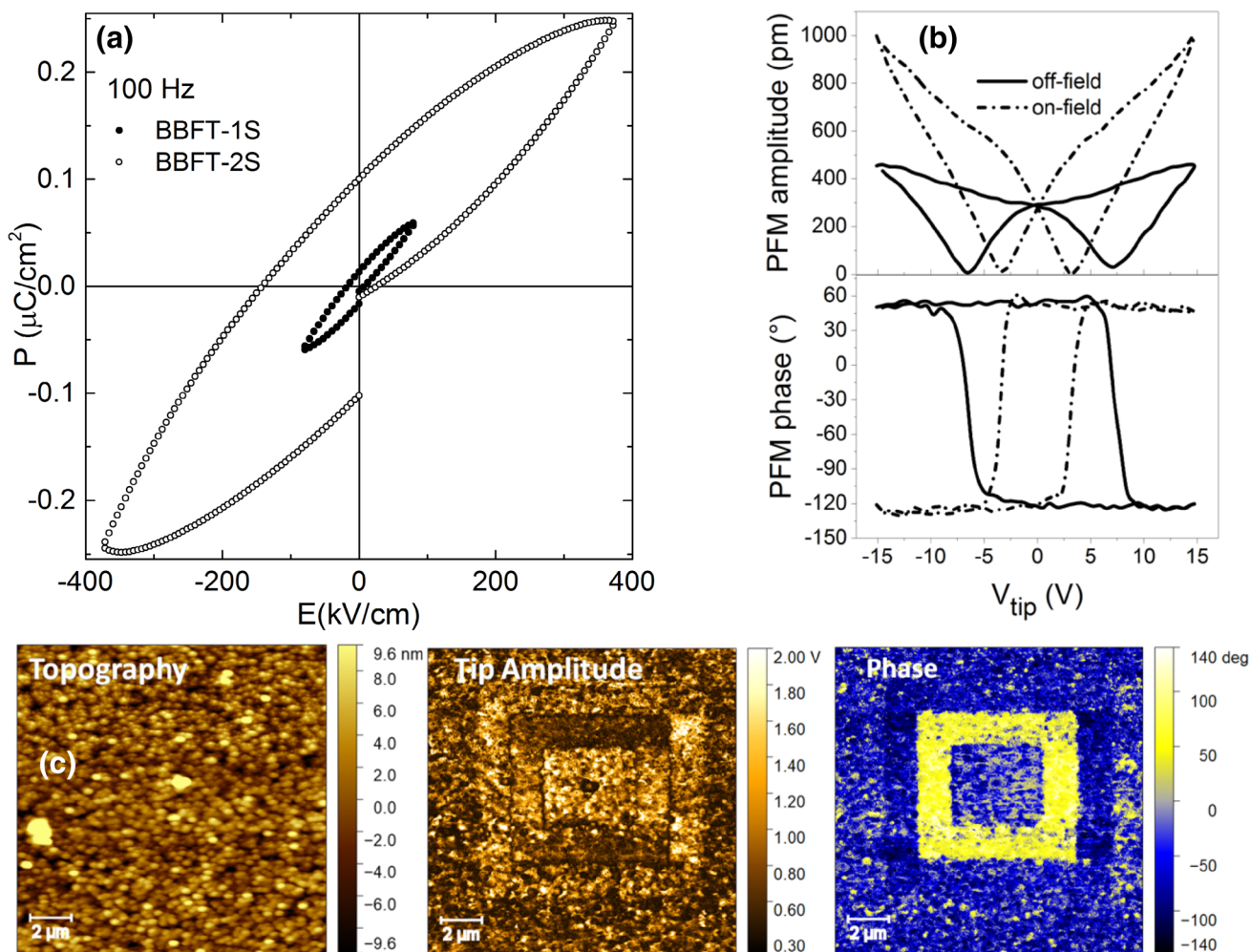


Fig. 6 **a** Ferroelectric hysteresis loops; **b** amplitude butterfly and phase-switching loops in the on-field and off-field for BBFT-1S; **c** topography, amplitude and phase images obtained through PFM measurements for BBFT-1S

magnetic properties of the film, typical of a canted spin ordered systems, are only slightly affected by the deposition route used. X-ray diffraction patterns, typical of BFO rhombohedral R3c perovskite structure, were observed for both films. From this technique, additionally, it may be concluded that there is a contraction of lattice parameters of the films compared to the bulk system. SEM micrograph reveals an improvement of grain morphology and surface quality for the film obtained by two-step deposition route. The ferroelectric nature of the studied films was confirmed through piezoresponse measurements.

Optical UV–vis experiments confirm a considerable increase in the optical band-gap of both films compared to its bulk counterpart. While from XPS results, it may be concluded a reduction in oxygen concentration defects in both films compared to bulk.

Finally, considering the improvement in morphology and surface quality of BBFT-2S, the increase of band-gap values, the ferroelectric hysteresis results and the reduction in oxygen defects compared to bulk systems, the selection of the two-step deposition route could become fundamental to obtain multiferroic BFO-based thin films with improved electrical properties.

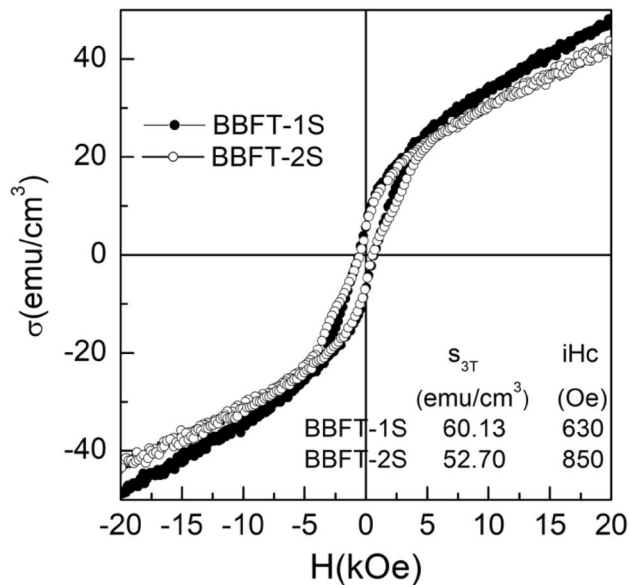


Fig. 7 Magnetic hysteresis loops

Acknowledgements The authors want to thank ICTP for financial support of the Latin-American Network of Ferroelectric Materials (NET-43, currently NT-02), to LIDTRA-CINVESTAV, Unidad Querétaro, for infrastructure facilities and to research assistants from CINVESTAV Ing. José Alfredo Muñoz Salas, Ing. José Eleazar Urbina Alvarez, Ing. Carlos Ávila and Ing. M.A. Hernández-Landaverde for their technical assistance. Dr. Osmany García and Dr. J. Martín Yáñez want to thank Sociedad Mexicana de Física for financial support. Dr. M.C. Rodríguez-Aranda acknowledges the financial support of Consejo Nacional de Ciencia y Tecnología (CONACyT) México, through Project CEMIESOL 22. FJFR acknowledges the support from FOINS—CONACyT Project 2016-01-2488.

References

1. S.J. Chiu, Y.T. Liu, G.P. Yu, H.Y. Lee, J.H. Huang, *Thin Solid Films* **529**, 85 (2013)
2. D.H. Wang, W.C. Goh, M. Ning, C.K. Ong, *Appl. Phys. Lett.* **88**, 212907 (2006)
3. D. Varshney, A. Kumar, K. Verma, *J. Alloys Compd.* **509**, 8421 (2011)
4. J. Silva, A. Reyes, H. Esparza, H. Camacho, L. Fuentes, *Integr. Ferroelectr.* **126**, 47 (2011)
5. G. Rojas-George, A. Concha-Balderrama, H. Esparza-Ponce, J. Silva, J.T. Elizalde Galindo, M.P. Cruz, J.J. Gervacio, O.A. Graeve, G. Herrera, L. Fuentes, A. Reyes-Rojas, *J. Mater. Sci.* **51**, 2283 (2016)
6. N.A. Spaldin, *Magnetic Materials Fundamental and Applications* (Cambridge University Press, Cambridge, 2010)
7. I. Sosnowska, T.P. Neumaier, E. Steichele, *J. Phys. C Solid State Phys.* **15**, 4835 (2000)
8. T.-H. Wang, C.-S. Tu, Y. Ding, T.-C. Lin, C.-S. Ku, W.-C. Yang, H.-H. Yu, K.-T. Wu, Y.-D. Yao, H.-Y. Lee, *Curr. Appl. Phys.* **11**, S240 (2011)
9. Y. Ma, W. Xing, J. Chen, Y. Bai, S. Zhao, H. Zhang, *Appl. Phys. A Mater. Sci. Process.* **122**, 1 (2016)
10. S. Díaz-Castañón, O. García-Zaldívar, J. Faloh-Gandarilla, B.E. Watts, F. Calderón-Piñar, M.A. Hernández-Landaverde, F.J. Espinoza-Beltran, *Appl. Phys. A Mater. Sci. Process.* **117**, 1283 (2014)
11. R.P. Laughlin, D.A. Currie, R. Contreras-Guererro, A. Dedigama, W. Priyantha, R. Droopad, N. Theodoropoulou, P. Gao, X. Pan, *J. Appl. Phys.* **113**, 111 (2013)
12. C. Lu, W. Hu, Y. Tian, T. Wu, *Appl. Phys. Rev.* **2**, 021304 (2015)
13. J.-M. Hu, C.-G. Duan, C.-W. Nan, L.-Q. Chen, *Npj Comput. Mater.* **3**, 18 (2017)
14. O. García-Zaldívar, S. Díaz-Castañón, F.J. Espinoza-Beltran, M.A. Hernández-Landaverde, G. López, J. Faloh-Gandarilla, F. Calderón-Piñar, *J. Adv. Dielectr.* **05**, 1550034 (2015)
15. A. Watcharapasorn, S. Jiansirisomboon, *Ceram. Int.* **34**, 769 (2008)
16. A. Tauc, J. Grigorovici, R. vancu, *Mater. Res. Bull.* **3**, 37 (1966)
17. C. Quan, Y. Han, N. Gao, W. Mao, J. Zhang, J. Yang, X. Li, W. Huang, *Ceram. Int.* **42**, 537 (2015)
18. M. Hernández-García, M.D. Durruthy-Rodríguez, J. Costa-Marrero, F. Calderón-Piñar, J.D.S. Guerra, J.M. Yáñez-Limón, *J. Appl. Phys.* **116**, 043510 (2014)
19. M.C. Rodríguez-Aranda, F. Calderón-Piñar, R. Mayén-Mondragón, J.M. Yáñez-Limón, *J. Mater. Sci. Mater. Electron.* **26**, 3486 (2015)
20. T. Mariño-Otero, M.A. Oliver-Tolentino, M.A. Aguilar-Frutis, G. Contreras-Martínez, E. Pérez-Cappe, E. Reguera, *Int. J. Hydrog. Energy* **40**, 5831 (2015)
21. L. Fang, J. Liu, S. Ju, F. Zheng, W. Dong, M. Shen, *Appl. Phys. Lett.* **97**, 95 (2010)
22. Y. Ren, X. Zhu, C. Zhang, J. Zhu, J. Zhu, D. Xiao, *J. Mater. Sci. Mater. Electron.* **26**, 1719 (2015)
23. Y. Ahn, J. Seo, J.Y. Son, J. Jang, *Electron. Mater. Lett.* **11**, 609 (2015)
24. A. Perejón, P.E. Sánchez-Jiménez, L.A. Pérez-Maqueda, J.M. Criado, J. Romero De Paz, R. Sáez-Puche, N. Masó, A.R. West, *J. Mater. Chem. C* **2**, 8398 (2014)
25. H. Yan, F. Inam, G. Viola, H. Ning, H. Zhang, Q. Jiang, T. Zeng, Z. Gao, M.J. Reece, *J. Adv. Dielectr.* **01**, 107 (2011)